Two-dimensional stokes flow around a heated cylinder: A possible application for diapirs in the mantle

R. Ziethe[1] and T. Spohn[2]

Received 6 October 2006; revised 13 April 2007; accepted 18 June 2007; published 18 September 2007.

[1] It is widely assumed that the separation of metal and silicates in a homogeneously accreted protoplanet occurred rather rapidly. The process of core formation through the descent of large, hot, iron-rich bodies through a cold, silicate protoplanet is discussed. If iron diapirs sink toward the planet center with the Stokes velocity, they would require more than 800 Ma to form a core in the case of a planet similar to the Earth. We therefore implement a temperature-dependent rheology for the silicate material surrounding the diapir, which leads to a reduction of the drag force exerted on the iron drop. We compare the drag force for different sinking velocities to the body force on the diapir and find that the terminal velocity in the temperature-dependent viscosity model is a factor of 30 higher than that in an isoviscous medium. On the basis of these results, the core formation time for the Earth could be as little as 30 Ma.

Citation: Ziethe, R., and T. Spohn (2007), Two-dimensional stokes flow around a heated cylinder: A possible application for diapirs in the mantle, *J. Geophys. Res.*, *112*, B09403, doi:10.1029/2006JB004789.

1. Introduction

[2] It is commonly accepted that the terrestrial planets and major moons are differentiated bodies with substantial iron cores. The core of the Earth has been proven to exist by seismological data. The presence of a Martian core has been inferred from the planet's gravity and precession rate data from the Mars Pathfinder mission [*Folkner et al.*, 1997; *Yoder et al.*, 2003; *Sohl and Spohn*, 1997]. Present data are insufficient to prove that Venus has a core, but its similarity to the Earth in terms of mass and radius suggests that its interior structure is also similar. The unusually high density of Mercury suggests that it has a substantial core [e.g., *Spohn et al.*, 2001]. Data on Mercury's surface gravity and precession rate are still unavailable, and must await future space missions such as Messenger (scheduled for arrival in 2011) and BepiColombo (to be launched in 2013, and scheduled for arrival in 2019). The gravity data gathered by the Galileo mission during flybys of Jupiter's principle satellites suggest that iron-rich cores are present in Io, Europa, and Ganymede (see *Sohl et al.* [2002] and *Schubert et al.* [2004] for recent reviews). Further evidence of a core in Ganymede can be found in its self-induced magnetic field, also detected by Galileo. The fourth major Jovian satellite, Callisto, is believed to be incompletely differentiated and probably has no iron-rich core. Although it is possible to construct models of the Moon that lack a core [e.g., *Kahn et al.*, 2000], a small core of about 400–500 km radius is accepted by most researchers in the field.

[3] We still lack a good understanding of the core formation process. Three mechanisms have been proposed to date (see *Stevenson* [1990] for a review) that allow iron to separate from silicate rock: the percolation of iron-rich melt through a solid silicate-rich matrix, iron-drop rainfall through a magma ocean, and negative diapirism following a Rayleigh-Taylor instability. In the percolation model, the planetary mantle is taken to be a porous medium containing finely distributed liquid iron. For sufficiently large permeabilities, the iron melt migrates through the silicate matrix to form larger bodies. This is possible if the dihedral angle θ of the melt pocket is smaller than 60°; larger angles will isolate the droplets and trap them in the solid. Unfortunately, the dihedral angle between iron melt and low-pressure (~3 GPa) silicate phases is commonly larger than 60° [*van Bargen and Waff*, 1986] so a continuous melt film is not likely. On the other hand, *Larimer and Herpfer* [1994] observed that the dihedral angle decreases in the presence of sulfur by an amount dependent on the concentration. *Bruhn et al.* [2000] demonstrated that shear deformation can help connect a significant fraction of initially isolated pockets of metal and metal sulphide melts in a solid matrix of polycrystalline olivine.

[4] The "rainfall" model assumes that the planet is largely molten after accretion. In a mass of liquid silicate molten iron can form drops up to about 1 cm in size [*Rubie et al.*, 2003], which sink downward to form a core at the center of the planet. Although this mechanism is straightforward, it is unlikely that terrestrial planets and smaller satellites could ever have been completely molten. The Moon is an exception; paleomagnetic data [*Stephenson et al.*, 1975] and isotope data [*Palme et al.*, 1984; *Wänke et al.*,

[1]Institute of Physics, University of Berne, Bern, Switzerland.
[2]Deutsches Zentrum für Luft- und Raumfahrt in der Helmholtz Gemeinschaft, Institut für Planetenforschung, Berlin, Germany.

0148-0227/07/2006JB004789$09.00

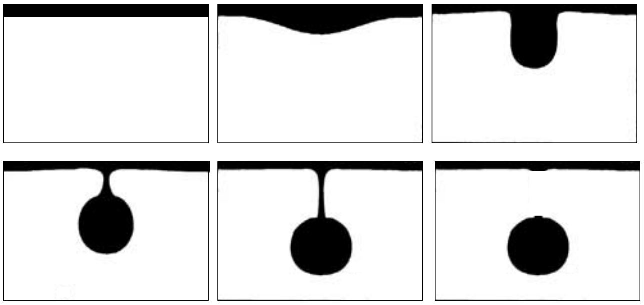

Figure 1. Sequence of different states of the formation and increase of a disturbance until a sphere-like body is detached. The material depicted in black denotes the specifically heavier material with the lower viscosity than the white material [after *Woidt*, 1978].

1977; *Münker et al.*, 2003] suggest that at least half its volume was once molten. This is probably a consequence of its formation from a hot vapor cloud created by a giant impact on the Earth. Nevertheless, the rainfall model might be applied to the separation of light and heavy compounds in a planet's magma ocean during the later stages of its accretion. It is very likely that an iron layer at the bottom of a magma ocean could be formed by the rainfall of iron drops.

[5] The third scenario considers the sinking of kilometer-sized iron bodies through the cold silicate mantle of a protoplanet. Large iron bodies may form from perturbations due to a Rayleigh-Taylor instability, or from the cores of predifferentiated planetesimals. Iron bodies collected during a protoplanets formation act as iron diapirs, which sink toward the center due to their density contrast with the mantle.

[6] It is very likely, that these mechanisms have worked in combination. For example, an iron-rich layer may form through rainfall at the bottom of a magma ocean. This layer may then trigger a Rayleigh-Taylor instability and negative diapirism. It is also possible, however, that a protoplanet forms from predifferentiated planetesimals [*Yoshino et al.*, 2003], whose individual corelets sink as diapirs.

[7] In this work we discuss the flow of the planetary mantle material around such objects. We evaluate the effects of a temperature-dependent viscosity on the behavior of the flow. Later on we apply the results to planetary core formation, for simplicity assuming a homogeneously accreted protoplanet.

2. Theoretical Background

[8] In this section we discuss the shape of the diapirs. We also explain why short core formation times cannot be obtained if the diapirs sink through a material with constant viscosity. Furthermore, we give a short introduction to the rheological model used in this paper and the calculation of the drag force, which is the key parameter that we need to evaluate.

2.1. Diapir Shape

[9] As mentioned in section 1, we assume that an iron layer at the bottom of a magma ocean is the source reservoir for the iron bodies. This is an unstable situation, because the density contrast between the iron layer and the silicate-iron mixture of the protoplanetary mantle is too high. The instability of a heavy fluid layer supported by a lighter one is known as a Rayleigh-Taylor instability [*Kull*, 1991]. The distortion of the interface between the fluids is reinforced by gravity, and will eventually lead to the growth of finger-like structures or even a complete overturn. In a system of two fluids with different material parameters, the shape of intrusions and interface distortions depends strongly on the viscosity contrast between the fluids [*Woidt*, 1978]. While there is a strong density contrast between the iron and the silicate material, the even stronger viscosity contrast is more important in determining the shape of the intrusions. The formation of intrusions due to a Rayleigh-Taylor instability has been investigated by numerous experiments [*Whitehead and Luther*, 1975] and numerical simulations [*Woidt*, 1978] in a geophysical context. The structural features of the growing interface instability are strongly dependent on the relative viscosities of the fluids. Designating the density of the top layer as ρ_1, its viscosity ν_1, the density of the bottom layer ρ_2 and the bottom layer viscosity ν_2 the structures can be divided into two categories. For $\rho_1 > \rho_2$ and $\nu_1 < \nu_2$, the intrusions will have a sphere-like shape; for $\rho_1 > \rho_2$ and $\nu_1 < \nu_2$, on the other hand, finger-like structures will occur. In the context of our problem the sinking iron bodies will be sphere-like, because $\rho_{Fe} > \rho_{Fe+Si}$ and $\nu_{Fe} < \nu_{Fe+Si}$, where the index Fe refers to iron, while Fe + Si refers to the underlying mixture of iron and silicate. Figure 1 illustrates the formation of a sphere-like intrusion.

2.2. Stokes Velocity in a Planetary Mantle

[10] Assuming that the viscosity of the material composing a protoplanet's mantle is constant, the time required for a diapir to reach the core can be estimated using the Stokes velocity (the terminal velocity of a sphere falling through a constant viscosity medium):

$$U_S = \frac{2}{9} \Delta\rho g \frac{r^2}{\mu} \tag{1}$$

with $\Delta\rho$ the density difference from the dipair to the surrounding medium, g the gravity acceleration, r the diapir's radius (here 5 km) and μ the viscosity of the surrounding medium. If we further assume that all iron diapirs have to move from a point close to the planet's surface to its center, the following core formation times result: Earth 824 Ma, Mars 2114 Ma, and Moon 259 Ma. The values for the parameters used to determine this times can be found in Table 1. The pure Stokes velocity is obviously far too slow to allow for the short core formation times (a few tens of million years for the Earth and Mars) suggested by *Stevenson* [1989]. Of course, if larger diapirs can be created, the Stokes velocity increases greatly. However, it is our intention to investigate not too large iron drops, since their sinking in due time is not questionable. In fact, we want to investigate, whether core formation is a rapid process, even if only small diapirs are present. Terminal velocities high enough for a 5 km diapir to reach the core in a reasonable time require viscosities lower than 10^{18} Pa s. It therefore seems reasonable to

Table 1. Parameters for the Numerical Model

Parameter	Symbol	Value
Temperature of the cylinder	$T_{\max}$	2800 K
Temperature of the surrounding fluid	T_0	1600 K
Gravitational acceleration	g	9.81 m s^{-2}
Density of the cylinder	ρ_{cyl}	7000 kg m^{-3}
Density of the surrounding fluid	ρ_f	4500 kg m^{-3}
Reference viscosity at 1600 K	ν_0	10^{21} Pa s
Specific heat	c_p	1000 J kg^{-1} K^{-1}
Thermal conductivity	k	4.7 W m^{-1} K^{-1}
Thermal diffusivity	κ	10^{-6} m^2 s^{-1}
Thermal expansion coefficient	α	10^{-5} K^{-1}
Activation temperature	A	10^4 K
Stress exponent	n	3

assume that core formation through negative diapirism in the mantle may result if the viscosity is temperature-dependent. The viscosity of the surrounding medium will then be reduced by the high temperature of the sinking diapir. Considering that the diapirs will have the temperature of molten iron, and knowing that planetary material has a strongly temperature-dependent rheology, it might be possible to increase even a small diapir's velocity enough for it to reach the planet's center within a reasonable time.

2.3. Rock Rheology

[11] The exponential dependence of the rock viscosity on the inverse temperature plays an especially important role in motion within a planetary mantle. We implemented the following viscosity law in our model [e.g., *Turcotte and Schubert*, 2002]:

$$\nu = \nu_0 \exp\left[\frac{A}{T_0}\left(\frac{T_0}{T} - 1\right)\right] \tag{2}$$

where A is the activation temperature, T_0 is a reference temperature taken to be the temperature far away from the diapir, T is the absolute temperature and ν_0 is the viscosity at the temperature T_0. Here we neglect the stress dependence of the viscosity for the sake of simplicity.

2.4. Drag Force

[12] The most significant feature of flow of a rigid body in steady translational motion through a fluid at rest at infinity is the total force exerted on the body by the fluid [*Batchelor*, 1981]. Contributions to this total force are made by the tangential stress at the body surface, integrated over that surface, and by the normal stress. The total force due to the tangential stress will be approximately opposite in direction to the velocity of the body. This is called the friction drag, because it is a consequence of viscosity or internal friction in the fluid. Note that the derivation of the equation for the drag force is done here only in two dimensions. This is due to the fact that the numerical solution can only be done two dimensional at the moment. We give more detailed reasons in section 3.1. In that case we are now treating a cylinder instead of a sphere here. We therefore refer more correctly to a cylinder from now on.

[13] If a boundary layer of thickness δ at the surface of an obstacle is considered, the velocity distribution in this boundary layer can be assumed to be linear [*Schlichting*, 1982]. Therefore the velocity is proportional to the distance y from the surface (see Figure 2 for illustration):

$$u(y) = \frac{y}{\delta} U \tag{3}$$

where U is the velocity outside the boundary layer. To keep the fluid moving along the cylinder's surface a tangential force τ is needed. This friction force per unit area (or unit length) is proportional to the velocity U and to the inverse thickness of the boundary layer δ [*Schlichting*, 1982]:

$$\tau = \nu \frac{\partial u}{\partial y} \tag{4}$$

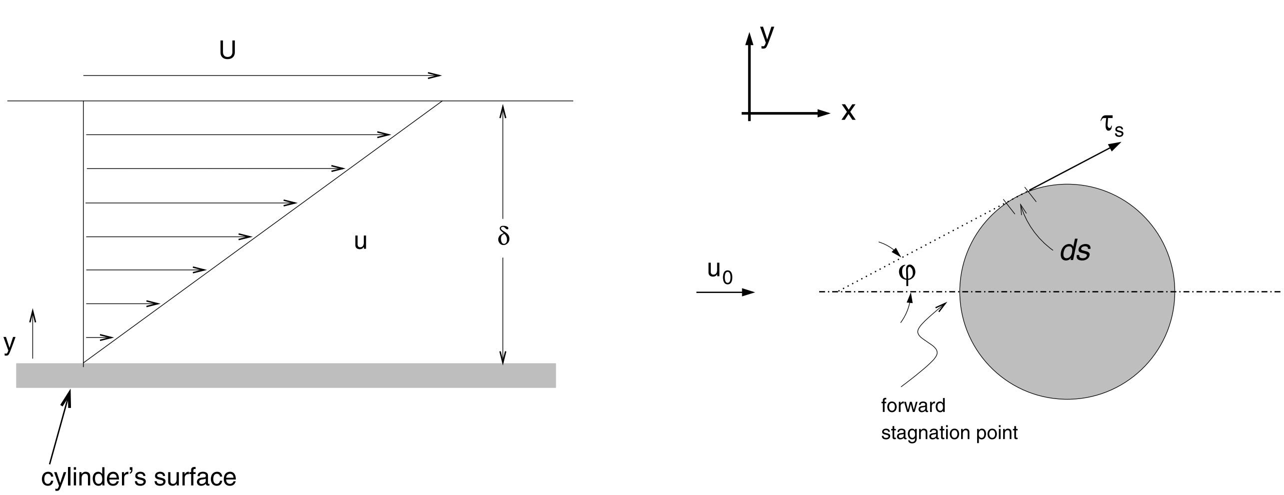

Figure 2. (left) Velocity distribution in a viscous fluid in the boundary layer at the obstacle's surface. (right) Illustration for the calculation of the drag force exerted on a rigid body in the steady flow of a fluid.

The proportionality factor between the velocity gradient and the tangential force is the viscosity. The friction force at the cylinder's surface is then (tangential surface force)

$$\tau_s = \nu \left(\frac{\partial u}{\partial y} \right)_{y=r_{diapir}} \tag{5}$$

To determine the drag force, the total force needed to move the fluid around the whole obstacle, the integral over the obstacle's surface of the tangential surface force must be computed [*Schlichting*, 1982]. In addition the normal force (pressure) must be taken into account. The drag force is then

$$F_D = 2r \int_{x=0}^{l} \left[\nu \left(\frac{\partial u}{\partial y} \right)_{y=r} + p_s \right] dx \tag{6}$$

with r the diapir's radius, ν the viscosity, u the velocity and p_s the normal force (pressure). The drag depends strongly on the shape of the body and the viscosity of the fluid. Any reduction of the viscosity will result in a reduction of the drag force.

3. Model Description

[14] Fluid flow around a body or obstacle is governed by the conservation of mass, momentum and energy:

$$\nabla \cdot \mathbf{u} = 0 \tag{7}$$

$$\rho(\mathbf{u} \cdot \nabla \mathbf{u}) = -\nabla p + \nabla \cdot \tau + \rho g \tag{8}$$

$$\frac{DT}{Dt} = \kappa \triangle T + \frac{\alpha g}{c_p} T \cdot \mathbf{u} + \frac{1}{\rho c_p} \tau \cdot \nabla \mathbf{u} \tag{9}$$

Here equation (7) represents the conservation of mass (continuity equation), equation (8) represents the conservation of momentum and equation (9) represents the energy conservation. In these equations, $\mathbf{u}$ is the velocity, ρ is the density, p is the pressure, τ is the stress tensor, T is the absolute temperature, κ is the thermal diffusivity, c_p is the specific heat capacity, and α is the thermal expansion coefficient. As described in sections 2.3 and 2.4, the sinking of large iron bodies (diapirs) through a silicate rock environment can be treated in terms of the creeping flow around an obstacle of a silicate fluid with variable viscosity. A diapir sinking toward the planet's center is affected by the frictional forces of the silicate material surrounding it (the drag force). The drag force is first evaluated for a range of velocities. By comparing the drag force found at each velocity with the body force, the terminal velocity can be determined. For each velocity a stationary solution of the flow will also be determined.

3.1. Numerical Solution

[15] The flow problem is studied using a software package called Featflow (Finite Element Analysis Tool), which was written by *Turek* [1998] to solve stationary and non-stationary flow problems for incompressible fluids. The package solves the stationary Navier-Stokes equation coupled to the mass and energy conservation and makes use of a multigrid algorithm (see *Wesseling* [1992] or *Trottenberg et al.* [2001] for details). A detailed view of the solver principle is given by *Schmachtel* [2003, and references therein]. An additional function was implemented to determine the temperature-dependent viscosity, which requires as further input the activation temperature A. Although the sinking bodies are probably spherical, in this work a cylindrical obstacle is used because no three-dimensional version of the program was available. The only difference between the drag force on a sphere and that on a cylinder is a constant geometry factor. Further the numerical results are obtained using a two-dimensional model, which is not directly comparable to the Stokes case for instance, which operates in three dimensions. We therefore corrected the results and give in principle the forces exerted on a cylinder, which mantle area is equal to that of a sphere with the same radius as the cylinder. The cylinders height has to be $h = 2r$ then, where the circular ends are not included, since they do not contribute to the drag force in the simulation. Of course there are still differences to a complete three dimensional model, but the drag force is the key parameter of this investigation. It is dominated by the surface area the fluid has contact with. Since this is not the same as for a sphere with the same radius, the errors of this study are not very important. We compared the drag force computed with the suggested approach to the Stokes forces and found a factor of 1.09 for the ratio $F_{\mathrm{Stokes}}/F_{\mathrm{drag}}$. The cylinder is placed in a channel (domain) which is large enough to avoid influences from the walls. To maintain the aspect ratio of the finite elements, we choose a cylinder radius which is 5% of the domain width. For a cylinder with 5 km radius, the domain is thus taken to be 100 km. Figure 3 (left) shows a schematic diagram of the "channel," cylinder, boundary conditions, and dimensions. Figure 3 (right) shows the (manually performed) discretization of this system into finite elements. The coarse grid contains 30 elements and 43 vertices (nodes). The elements are smaller close to the cylinder than at the channel's borders, because it is there we expect the steepest gradients of the flow velocity, pressure, temperature, and viscosity to occur. Far away from the cylinder the flow does not change very rapidly, so the elements can be larger. The coarse grid needs to be refined for the purposes of simulation, which is done automatically by the finite element program.

[16] The velocity components $u_x = u_{x0}(x, y)$ and $u_y = u_{y0}(x, y)$ are input parameters which are set initially. In addition conditions at the boundaries are needed. The velocity component perpendicular (or "normal") to the boundary is called u_n and the component tangential to the boundary u_t. The inflow condition is given for both velocity components:

$$\begin{aligned} u_n(x, y=0)\Big|_{\Gamma_1} &= u_{n0} = u_0 \\ u_t(x, y=0)\Big|_{\Gamma_1} &= u_{t0} = 0 \end{aligned} \tag{10}$$

for known values for u_{n0} and u_{t0} (inflow velocities at the bottom of the channel). Γ_1 is the outer boundary of the area and Γ_2 is the inner boundary, the cylinder's surface.

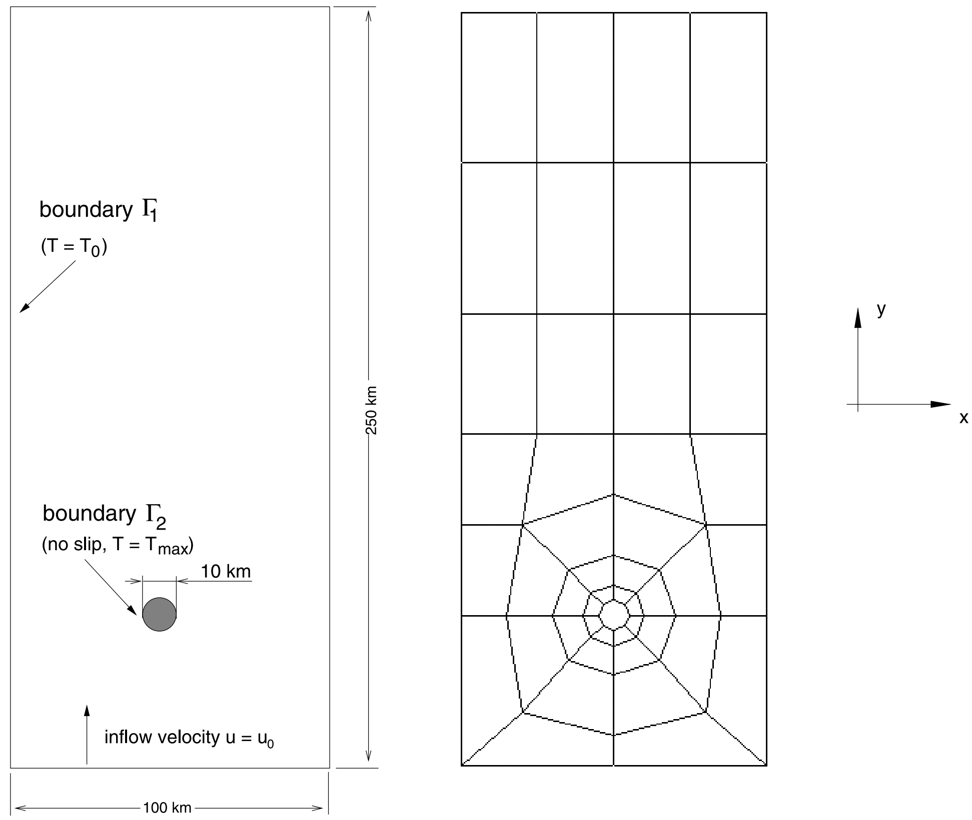

Figure 3. (left) Model setup of a single cylinder. The boundary conditions and dimensions are marked in the figure. (right) Manually performed coarse discretization into finite elements.

Compare with Figure 3 for illustration. For the outflow condition the velocity components should not change in the direction perpendicular to the wall:

$$\frac{\partial u_n(x, y = y_{\max})}{\partial n} = 0$$
$$\frac{\partial u_t(x, y = y_{\max})}{\partial n} = 0 \tag{11}$$

We also assume a "no-slip" condition at the interface between the cylinder and the fluid:

$$u_n(x,y)\Big|_{\Gamma_2} = 0$$
$$u_t(x,y)\Big|_{\Gamma_2} = 0 \tag{12}$$

Along the outer boundaries of the area we use a "quasi-free-slip" condition: The outer boundary is assumed to be so far away from the cylinder that the velocity field is undisturbed, so the velocity is equal to inflow velocity:

$$u_n(x=0,y)\Big|_{\Gamma_1} = u_n(x = x_{\max}, y)\Big|_{\Gamma_1} = 0$$
$$u_t(x=0,y)\Big|_{\Gamma_1} = u_t(x = x_{\max}, y)\Big|_{\Gamma_1} = u_0 \tag{13}$$

We use a "Dirichlet" boundary condition for the temperature:

$$T\Big|_{\Gamma_2} = T_1 \tag{14}$$

meaning that the temperature of the cylinder is given. The model does not allow to use time-dependent function for T_1 and hence T_1 is taken to be constant. This might seem a bit unrealistic, since the diapir would cool as it sinks and the effect of its temperature on the viscosity would decrease. Under such conditions the diapir would slow down, and rapid core formation would be impossible. However, the cooling might also be ineffective and the release of potential energy during the settling process prevents the diapir partially from cooling. A proper energy balance is part of future work. The constant temperature is discussed in more detail in section 6.

3.2. Parameter Values

[17] The purpose of this paper is to answer general questions about planetary core formation, so the choice of parameters should not be restricted to a particular planet. We assume that some parameters are independent of the size, mass, chemistry, and general structure of a planet. The Earth provides the best available estimates of such parameters, so these values are adopted. Table 1 lists the relevant parameters and their values.

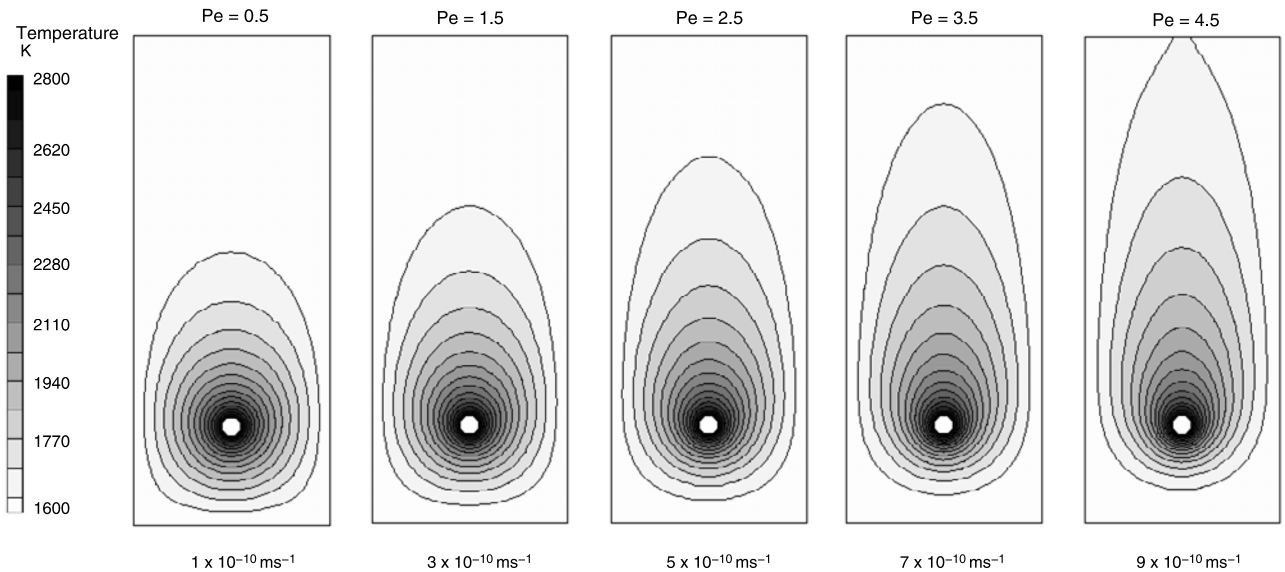

Figure 4. Temperature distribution around a heated circular cylinder at different sinking velocities. The flow transports the heat of the cylinder in its wake. The ratio between conduction and advection of heat determines the shape of the wake. For low sinking velocities the wake is wider and shorter. For high velocities the role of conduction is reduced, and therefore the wake is longer and more narrow.

[18] The cylinder temperature is set to 2800 K to simulate a hot, liquid iron diapir above its melting temperature. The melting temperature of iron is 1812 K at standard pressure [*Holleman and Wilberg*, 1985; *Stöcker*, 1994]. We assume that the iron settled to the bottom of a magma ocean, created during the "heavy bombardment" period when even silicate material was melted due to the conversion of impact kinetic energy into heat [*Zahnle et al.*, 1988] give temperatures ranging from 900 K to over 3000 K for the interior of a freshly accreted planet. Because the temperature shortly after a planet's accretion is not known exactly, the iron temperature is set to 2800 K. [*Rubie et al.*, 2003] use temperatures up to 3000 K for the bottom of the terrestrial magma ocean. For the temperature far away from the diapir we chose values between 1600 K and 2200 K. For ambient temperatures smaller that 1600 K the diapir needs to "burn" its way through the surrounding material and the thermal conductivity is the most important parameter. For ambient temperatures above 2200 K the effects of the temperature dependence of ν are relatively minor.

[19] The density of the cylinder is set to a value of 7000 kg m^{-3}, which is nearly the density of pure iron, which would be 7873 kg m^{-3} (according to *Holleman and Wilberg* [1985]). Planetary iron is quite often contaminated with lighter siderophile elements. One of the most common contaminants is sulfur, which combines with iron to make the compound FeS. The density of this compound depends on the amount of sulfur present [*Balog et al.*, 2003]. It is assumed in this work that the iron was only mildly contaminated with lighter elements, and thus a density of 7000 kg m^{-3} is used for the diapirs contributing to core formation.

[20] A density of 4500 kg m^{-3} is used for the fluid surrounding the cylinder, which is the value [*Lodders and Fegley*, 1998] give for the Earth's mantle today. This assumption is somewhat crucial, because the mantle of a planet will certainly evolve quickly after accretion. If the planet accreted homogeneously [*Righter and Drake*, 1996], then the early mantle probably contained iron as well as silicates, which would increase its density. Since the nature of accretion is not well known, however, we simply adopt the Earth's current mantle density as the density of the fluid surrounding the cylinder. This value is somewhat higher than the mantle densities of the other terrestrial planets, so is perhaps closer to an iron-silicate mixture than a pure silicate.

[21] The reference viscosity of the fluid is 10^{21} Pa s, which is similar to the present-day mantle viscosity of the Earth [*Cathles*, 1975; *Stevenson et al.*, 1983]. This value is used as the "background" viscosity for the material at a temperature of 1600 K.

[22] The values for the specific heat c_p and the thermal expansion coefficient α were also chosen to match their present-day value for the Earth's mantle [*Turcotte and Schubert*, 2002]. Using a thermal conductivity k = 5 W m^{-1} K^{-1} [*van den Berg et al.*, 2001; *van den Berg and Yuen*, 2002] the resulting thermal diffusivity is about 1.0×10^{-6} m^2 s^{-1}.

4. Results

[23] In this section the results of several numerical simulations are presented and discussed.

[24] In Figure 4, temperature distributions around a heated cylinder for a range of sinking velocities are shown. The highest temperatures, of course, are observed at the surface of the cylinder. The heat is transported with the flow into the wake of the cylinder. The shape of this temperature wake depends strongly on the flow velocity $\mathbf{u_0}$ and the thermal diffusivity of the surrounding material. As expected, the wake is wider for lower sinking velocities and narrower and longer for higher velocities. The driving force behind

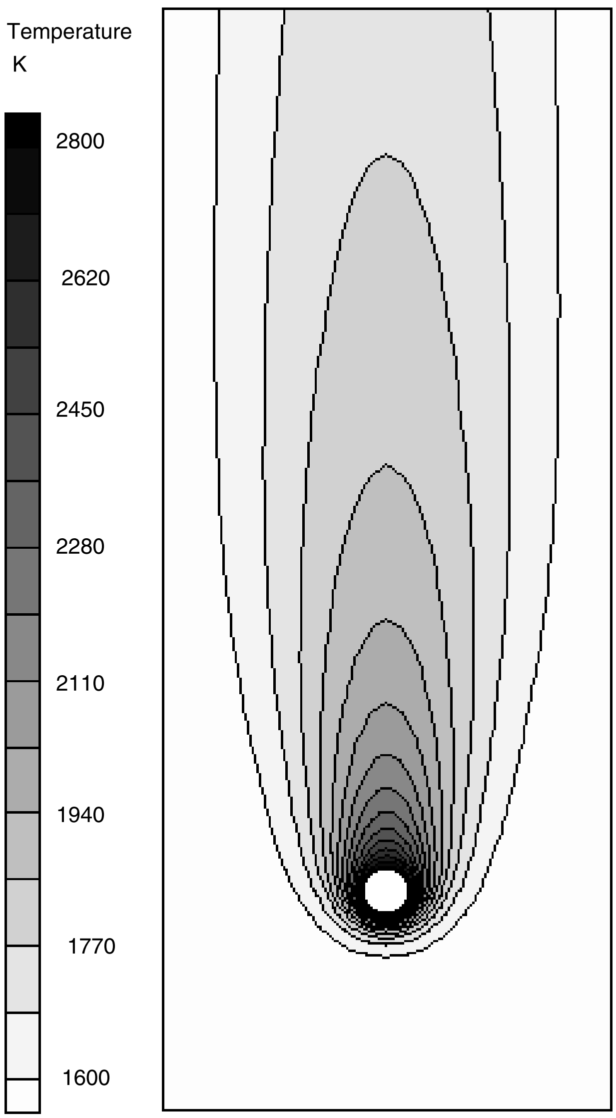

Figure 5. Temperature distribution around a heated circular cylinder. The flow transports the heat of the cylinder in its wake and produces a channel of higher temperature. Initial temperature difference between cylinder and surrounding is 1200 K, inflow velocity is 2.0×10^{-10} m s^{-1}, and the activation temperature A is 10^4 K.

these different shapes is the ratio between advection and heat conduction, usually expressed as the Péclet number Pe. This is defined as

$$Pe = \frac{uL}{\kappa} \tag{15}$$

where u is the sinking velocity, L is a characteristic length (e.g., the cylinders radius), and κ is the thermal diffusivity. When Pe is small, the flow has negligible effect on the temperature distribution because κ is then the dominant parameter. When Pe is large, conduction is only important in the thermal boundary layers. In this scenario, the flow velocity is dominant. This can be seen in Figure 4, where the area of temperatures above 1600 K in front of the forward stagnation point is wider for low sinking velocities. Figures 5 and 6 show the temperature and viscosity distributions around a heated cylinder, respectively. The material is less viscous at higher temperatures, so we also find the smallest viscosities at the cylinder's surface. The heat of the cylinder is transported into its wake, so the high-temperature channel also has lower viscosity as shown in Figure 6. This phenomenon can cause several different effects. The low viscosity at the cylinders surface leads to a reduction of shear forces in the friction layer, which increases the velocity of the cylinder. This also has an effect on any diapirs that follow the first one in the same area. Because the first cylinder leaves a low-viscosity channel, following cylinders may sink faster than the first one.

[25] Friction forces also cause a pressure gradient along the surface of the cylinder, which is necessary to move the fluid adjacent to the surface against the shear forces. A lower viscosity at the cylinder's surface reduces the shear forces and therefore also the drag force. The drag force consists of the friction at the cylinder's surface (a surface integral of the deviatoric stresses) and the pressure force (a surface integral of the normal forces) [*Schlichting*, 1982]. Figure 7 shows the drag force as a function of sinking velocity for two constant viscosity cases and for the temperature-dependent case. The isoviscous cases are generated by evaluating equation (2) at fixed temperatures: For the "cold" case we have a viscosity of $\nu(T = 1600) = \nu_0 = 10^{21}$ Pa s, and for the "hot" case we use a viscosity of $\nu(T = 2800) = \nu_0 = 6.87^{19}$ Pa s. The values for the drag force are normalized to the Stokes force

$$F_s = 6\pi\rho_{sil}\nu a \tag{16}$$

where U_s is the Stokes velocity, which is computed according to equation (1). The values for the velocity are also normalized to Stokes velocity. As expected, the drag force exerted on the diapir is significantly smaller when the material has a higher temperature; at the highest possible temperature in this model (2800 K), the viscosity is reduced by a factor of about 1800. In a temperature-dependent rheology, the drag force on a body moving through the material is smaller than that in a "cold" rheology but higher that in a "hot" rheology. Although close to the diapir the temperature is highest and the viscosity is lowest, the body moves slower than it would through a completely hot medium. This is due to the fact that the momentum diffusion length is much larger than the thermal diffusion length. The cylinder therefore "feels" the presence of colder and more viscous areas far away from it.

[26] Although the drag force increases with velocity the ratio between the drag forces remains constant, at least in the range numerically investigated. For the constant viscosity cases this is, of course, to be expected.

[27] Knowing the equation for the body force (for a spherical body with radius a)

$$F_B = mg = \frac{4}{3}\pi a^3 \Delta\rho g \tag{17}$$

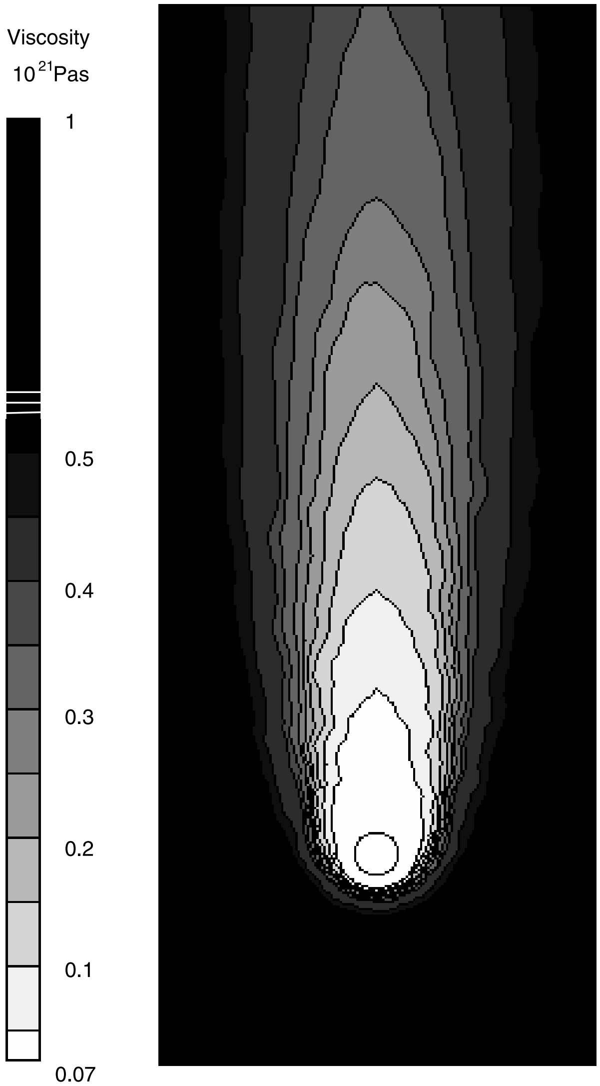

Figure 6. Viscosity distribution around a heated circular cylinder. Because of the temperature dependence of the viscosity, there is a channel of lower viscosity in the cylinder's wake analogous to the channel of higher temperature. Parameters are the same as in Figure 5.

where m is the mass of the body in the gravitational field at the surface of a planet, a is the radius, $\Delta\rho$ is the density difference between the body and the surrounding material and g is the planet's gravitational acceleration, the terminal velocity of a body moving through the silicate rock mantle of a planet can be calculated. The terminal velocity is defined as the velocity at which the body force is equal to the drag force. In Figure 8, the drag forces for the cold, isoviscous case and temperature-dependent case are compared to the body force. For the purposes of comparison, the terminal velocity of a 5 km radius sphere can also be calculated using the Stokes equation [e.g., *Sommerfeld*, 1992]. The Stokes velocity is then 1.36×10^{-10} m s^{-1}. Our code slightly underestimates the friction forces, the factor $F_{\mathrm{stokes}}/F_{\mathrm{code}}$ is 1.09. This id due to geometry, as mentioned above, out code operates only in two dimensions. Since the difference between the forces for spheres and cylinders is in this regime almost negligible we use the body force for a sphere here. The intersection of the body force curve and the drag force curve (both normalized to the Stokes force denotes the point, where the velocity reaches its maximum and is therefore called terminal velocity. As expected we find a higher terminal velocity for the temperature-dependent case (7×10^{-9} m s^{-1}), which is approximately 30 times higher than in the isoviscous case. The velocity increase can directly be seen at the x axis in Figure 8 because the velocity is normalized to the Stokes velocity. For the isoviscous cold case the intersection between body force and drag force occurs at 1 in Figure 8.

[28] Figure 9 shows the drag force as a function of the sinking velocity (again normalized to Stokes force and velocity, respectively), for values of the activation temperature in equation (2) ranging from 1000 K to 10,000 K. The viscosity contrast between the far-field viscosity ν_0 and the viscosity $\nu(T_2)$ at the surface of the cylinder increases from a factor of 1.3 for $A = 1000$ to a factor of 14 for $A = 10{,}000$. For a fixed sinking velocity, the drag force decreases with increasing activation temperature. Since the activation temperature is a measure of the strength of the temperature dependence, this result was to be expected. It means that the viscosity's temperature dependence increases with the activation temperature A as the slope of the viscosity function is generally negative. As the activation temperature increases, the velocity profile is confined to progressively narrower regions near the cylinder's surface. There are two competing effects of the temperature dependence of the viscosity on the drag force (compare equation (6)): The reduction of the drag force due to the decrease of the viscosity will be partly compensated by an increase in the gradient in the velocity. For very large values of A most of the fluid moves at the velocity of the cold fluid, while the drag force is only reduced in a relatively hot, low-viscosity layer adjacent to the cylinder's surface. The outer part of the model volume behaves as if it were almost entirely rigid in this case. In Figure 10 it can further be seen that for increasingly high activation temperatures the drag force decreases less and

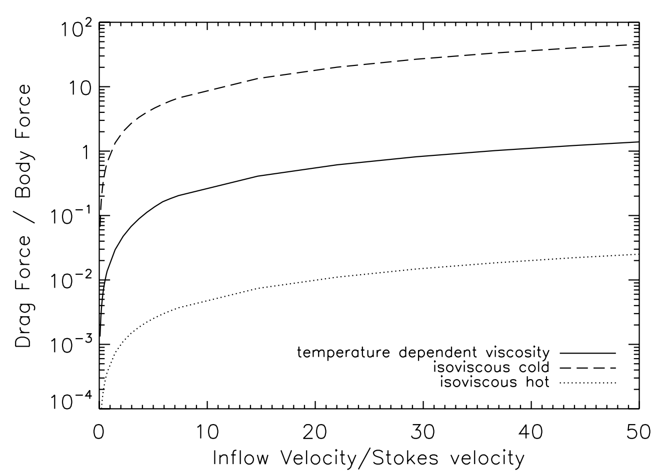

Figure 7. Drag forces on a cylinder with 5 km radius depending on its sinking velocity for different viscosity cases. Dashed line, $\nu = \nu(T_0)$ ("cold case"); dotted line, $\nu = \nu(T_{\mathrm{max}})$ ("hot case"); solid line, temperature-dependent viscosity (equation (2)).

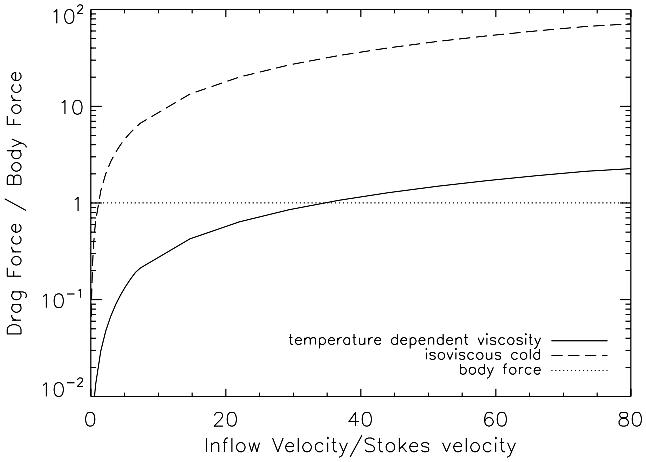

Figure 8. Drag force depending on the sinking velocity for the isoviscous (cold) case (dashed line) and the temperature-dependent case (solid line). The body force is the dotted line parallel to the x axis. The points where the body force line intersects with the drag forces correspond to the terminal velocities for the considered rheologies.

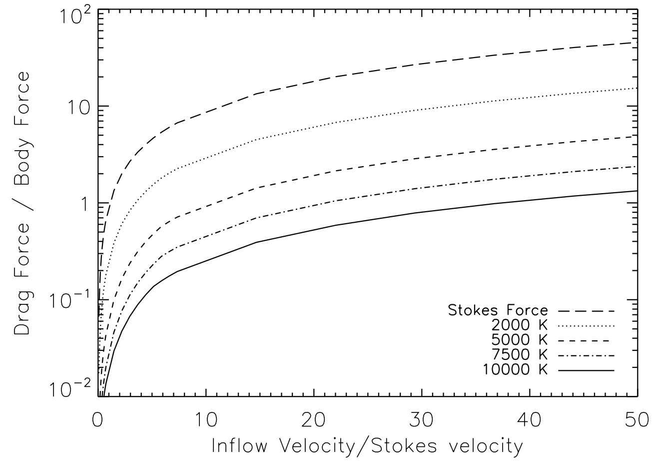

Figure 9. Drag forces depending on the sinking velocity for different activation temperatures (solid line, $A = 2000$ K; dotted line, A = 5000 K; dashed line, A = 7500 K; dash-dotted line; A = 10,000 K). The minimum temperature is T_0 = 1600 K, and the temperature of the cylinder's surface is 2800 K.

less quickly. This is more or less independent from the velocity of the object, as can be seen Figure 10, since the curves for different velocities are very close to each other. One can expect that values above A = 10,000 K will not further decrease the drag force to a significant degree. The activation temperature for a typical mantle material such as olivine could easily be a factor of 4 or 5 higher, but for numerical reasons only the value A = 10,000 K could be modeled. Figure 11 shows an extrapolation of our data. We fitted a function ($F_D = 6 \times 10^{15} e^{(-0.0004x)}$) to the data computed with our model in order to find out, how the results would change, if an activation temperature of 40,000 K would be used. According to this function the drag force is reduction is a few orders of magnitude stronger than for an activation temperature of 10,000 K. However, there are only eight data points to fit a function to, which keep the correlation coefficient at only 0.956. We therefore think that the strong reduction of the drag force at higher activation temperatures that used in our model, is somewhat overestimated. However, one has to keep in mind that the terminal velocities would be higher and estimated core formation times would be lower than suggested by our model.

[29] Figure 12 shows the drag force as a function of flow velocity normalized to Stokes force and velocity, respectively) for different cylinder temperatures. For a fixed sinking velocity, the drag force is significantly higher for smaller values of the cylinder temperature. This behavior can be explained by considering that the coldest areas have viscosity $\nu(T = T_0 = 1600 \text{ K}) = \nu_0$. The colder the cylinder's surface, the lower the viscosity contrast between the far field and the cylinder's surface will be. For a cylinder temperature of 1600 K there is no viscosity contrast, and we revert to the isoviscous, "cold" rheology where all material has the viscosity ν_0. Higher cylinder temperatures result in smaller T_0/T ratios in the viscosity law (equation (2)), and lower viscosities in the hot areas. Because lower viscosity values result in lower shear forces and therefore lower drag forces, the lowest drag forces for a fixed sinking velocity are observed for high cylinder temperatures. This means that a hotter cylinder is able to move faster than a cold one through a medium at any given temperature, provided that the medium has a temperature-dependent rheology. Further increases in the surface temperature of the cylinder will decrease the drag force even more, but as $T_0/T \rightarrow 0$ the viscosity goes to

$$\lim_{T\to\infty} \nu = \nu_0 \exp\left[-\frac{A}{T_0}\right] \tag{18}$$

Evaluated for $\nu_0 = 10^{21}$ Pa s, A = 10,000 K and T_0 = 1600 K, equation (18) yields 1, 93 $\times$ 10^{18} Pa s corresponding to a viscosity contrast on the order of 10^3.

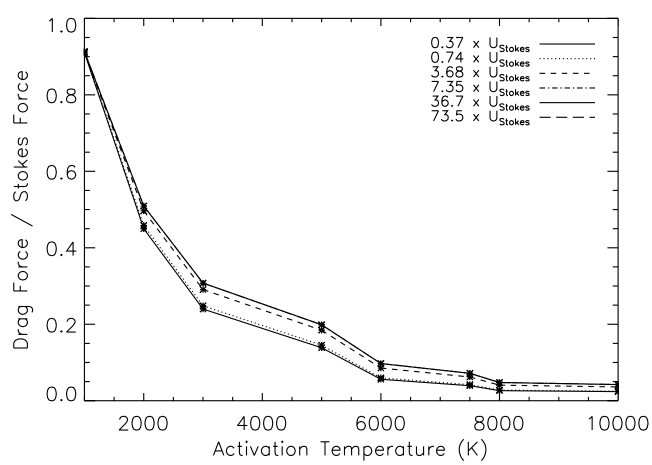

Figure 10. Drag forces depending on the activation temperature at various velocities. The drag force is smaller for higher values of the activation temperature. However, the higher the value of A, the less effective seems the drag force reduction due to the temperature dependence of the viscosity.

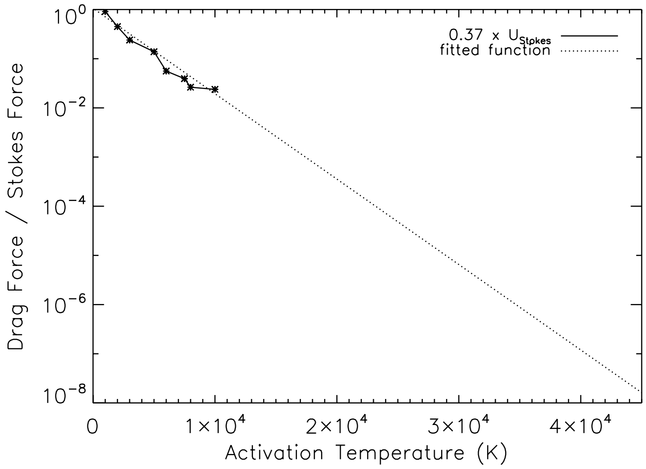

Figure 11. Drag forces depending on the activation temperature. The solid line with symbols are the computed values, and the dashed line corresponds to a the function chosen to fit the data reasonably well (see text). Note that the y axis is logarithmic.

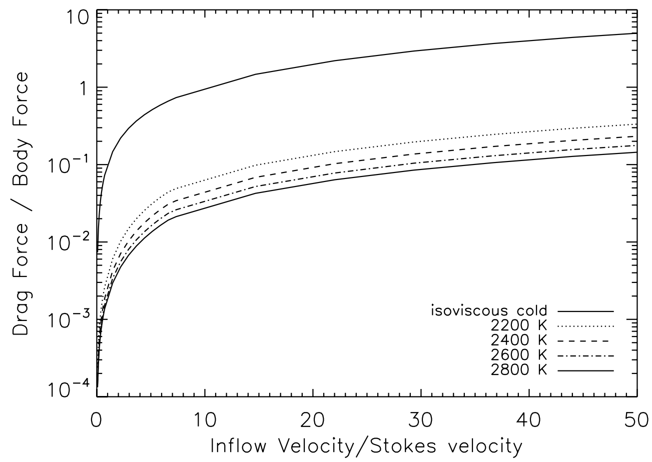

Figure 12. Drag forces depending on the sinking velocity for different temperatures of the cylinder's surface. The minimum temperature of the surrounding is T_0 = 1600 K, and the activation temperature is A = 10,000 K.

[30] Figure 13 shows the drag force as a function of the sinking velocity (normalized to Stokes force and velocity, respectively), for various temperatures of the surrounding material. The cylinder itself has a fixed temperature of 2800 K, and the reference viscosity ν_0 is 10^{21} Pa s. We see that the drag forces are generally higher when the material surrounding the cylinder is colder. When the temperature of the surrounding material is 2800 K, on the other hand, there is no temperature difference between and we recover the case of an isoviscous, "hot" rheology with a viscosity of $\nu = \nu(T = T_0 = 2800\ \mathrm{K}) = 6.87 \times 10^{19}$ Pa s. This means that the cylinder moves faster through a hot (and therefore soft) medium than through a cold one, which is not unexpected. Looking at Figure 13, we also see that the function for T_0 = 1600 K is more strongly curved than the functions for higher environment temperatures. This is due to the stronger viscosity contrast, even though the rest of the fluid has a relatively high viscosity. Higher temperatures also lower the far field viscosities from the beginning.

[31] Figure 14 shows the drag force as a function of the flow velocity, for cylinders with different radii. The temperature of the cylinder is set to 2800 K, the temperature of the far field T_0 to 1600 K, the activation temperature A to 10,000 K, and the reference viscosity ν_0 to 10^{21} Pa s. Exactly as expected, the drag forces are higher when the cylinder has a larger radius. The points in Figure 14 denote intersections of the corresponding body force curves (which would be lines parallel to the x axis) with the drag force curve, and mark the terminal velocities of the various cylinders. It can clearly be seen that the terminal velocity of a cylinder is higher for larger radii. Figure 15 shows the relationship between the ratio of the terminal velocity to the Stokes velocity (x axis) and the ratio of the cylinder's surface area to its volume (y axis). Note that we use our special cylinder for determining this ratio, where the circular areas at the ends are excluded. Basically the ratio of surface area A' to volume V is then $A'/V = 2/r$. The black line is the result of a linear regression on the data points, which represent the computed results. The linear relationship between these two ratios is clear. The high ratio of surface area to mass is the reason for the large difference between the observed terminal velocity and Stokes velocity in small cylinders. Small cylinders do not achieve a high terminal velocity compared to large cylinders, but the difference between their actual velocity and Stokes velocity is much higher for smaller objects.

5. Discussion

[32] The determination of the drag force, the body force and the terminal velocity have turned out as the key features in the investigation of a cylinder in the flow with different rheological properties. For a constant viscosity of the medium we found the typical results that were expected from the Stokes theory for spheres (terminal velocities are

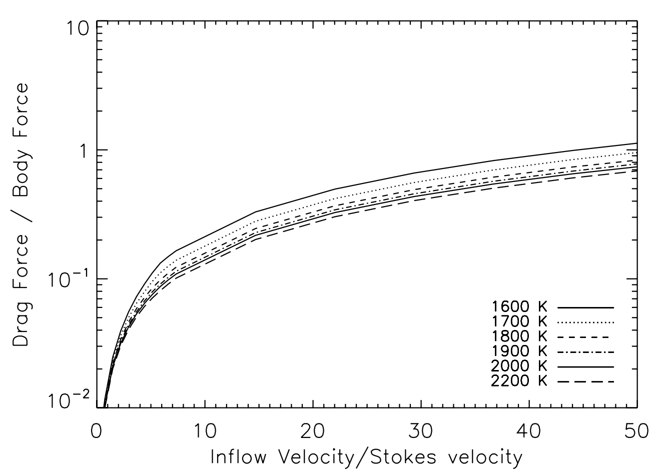

Figure 13. Drag forces depending on the sinking velocity for different temperatures of the surrounding fluid. The surface temperature of the cylinder is 2800 K, and the activation temperature is A = 10,000 K. The reference viscosity is still the viscosity for a temperature of 1600 K.

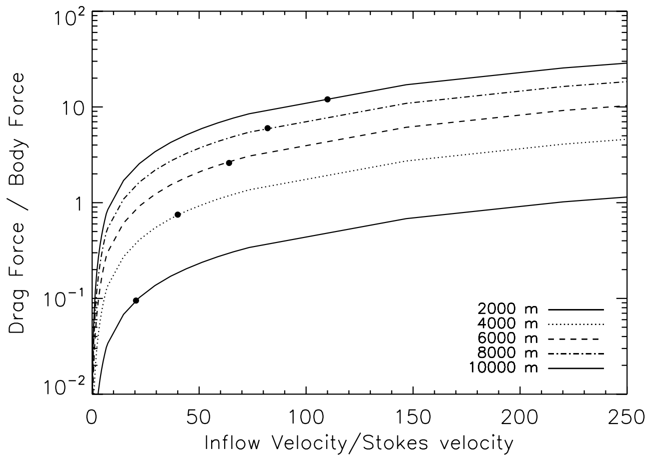

Figure 14. Drag forces depending on the sinking velocity for different cylinder radii. The points mark the intersection between the drag force curve and the body force for the cylinders, respectively.

overestimated by our model by a factor of 1.5). Applying a temperature-dependent viscosity changes the results for the drag force exerted on an object in the flow significantly. The drag force is reduced by 1–2 orders of magnitude. The terminal velocity derived by equating the constant body force to the drag force results in a velocity that is roughly 30 times higher than the corresponding terminal velocity for the cylinder in a constant viscosity medium. Applied to the problem of planetary core formation by sinking hot iron diapirs, this helps to increase the diapir velocity. As pointed out in section 1, the settling of iron spheres in silicate rock material for high viscosities of the planetary mantle might become frustrated. The diapirs have to be rather large to achieve a velocity high enough to reach the planet's center within a short timescale (in the order of 10 Ma for the Earth or shorter, see section 1). A temperature-dependent rheology leads to a sufficient reduction of viscosity to increase the terminal velocity of a diapir. If we apply the results to the Earth, we find that a diapir with a radius of 5 km would have a terminal velocity (equal to its Stokes velocity) of 2.45×10^{-10} m s^{-1} and would therefore need 824 Ma to arrive at Earth's center, if the viscosity of the Earth's mantle would be constant. Larger diapirs have a larger terminal velocity, but to reach the Earth's center in 30 Ma the diapir has to be larger by 1 order of magnitude (50 km would be sufficient). It remains questionable whether diapirs that large can form. Even if it is possible, there would probably still remain a sufficiently large amount of iron that forms smaller diapirs, which might stay in suspension and then would have no chance to contribute to the iron core. The reduced viscosity decreases the traveltime to the core for the 5 km model diapir by more than 1 order of magnitude. Assuming that the terminal velocity of the diapir is representative for all diapirs contributing to the Earth's core, our core formation time of roughly 30 Ma is already a good estimate.

[33] Under the very rough assumption that the Moon and the Mars have the same bulk composition and differ from the Earth only in the gravitational acceleration, the body forces for the Moon and the Mars can be calculated and the terminal velocity of 5 km sized diapirs can be derived. Table 2 shows the results for the corresponding core formation times for the Earth, Mars, and Moon compared to the Stokes velocity. This analysis does not account for the different densities of the mantle or the cores of the planets. Further investigations with a different parameter range might result in core formation times, which are even shorter. [*Stevenson*, 1989] suggested a timescale of roughly 1 Ma. We conclude that the method used in this work is therefore applicable to core formation in terrestrial planets in general and not only for the Earth. Of course, the model is rather simple at the moment. It was tested, whether there is a possibility to simulate a process like planetary core formation. We see already a lot of points, where the model and the software can be improved. Future work will include massive software development in order to come closer to a realistic simulation of core formation.

[34] The investigation of the parameters governing the viscosity law provided the expected results. The variation of the activation temperature showed that the drag force reduction is stronger for higher values of A. This can be explained by the stronger temperature dependence of the viscosity, if the activation temperature is higher. The used activation temperature value is probably too small due to numerical reasons, but our results show that the implementation of higher values of A would even reduce the drag force and therefore increase the terminal velocity.

[35] Because the temperature of the interior of the protoplanets is still not well known, we varied the temperature of the material surrounding the cylinder. As expected the terminal velocity increases if the temperature becomes higher. A diapir can sink faster through a hot planetary mantle than through a cold one. Since a relatively low value for the temperature of the material surrounding the diapir

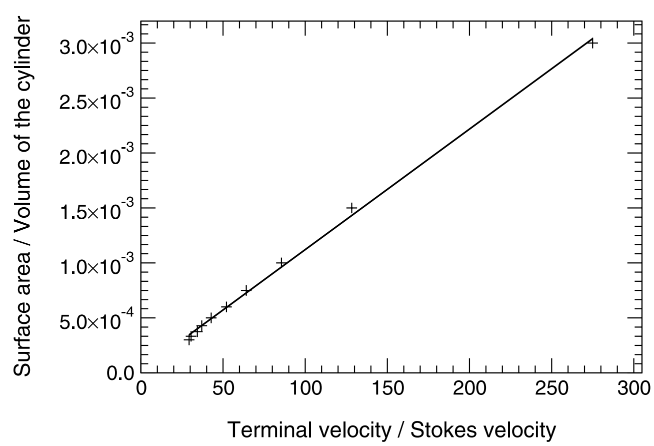

Figure 15. Ratio of surface area to volume in dependence of the ratio of terminal velocity to Stokes velocity. The crosses denote the computed values, and the solid line is a linear regression of those values. The velocity increase compared to the Stokes velocity is higher for small cylinders because of their large surface area compared to their volume. The temperature of the cylinders is taken to be 2800 K, the temperature in the far-field T_0 is 1600 K, the activation temperature A is 10,000 K, and the reference viscosity ν_0 is 10^{21} Pa s.

Table 2. Core Formation Times for Terrestrial Planets

Planet	This Work	Stokes
Earth	30 Ma	824 Ma
Mars	40 Ma	2114 Ma
Moon	40 Ma	259 Ma

was chosen here, we could show that even for such a cold case the diapir becomes fast enough to reach the planet's center within a reasonable time. Even if the temperature assumptions were still too optimistic, and the deep interior of a freshly accreted planet is cooler than 1600 K, this is probably only valid for a relatively small region in the very center. According to *Breuer* [2003], *Zahnle et al.* [1988], and *Safronov* [1978] it is more probable that the planets become hot during the late stages of accretion or shortly after their accretion.

[36] Similar to the results for the variation of the surrounding temperature, we found that the drag force reduction is higher, if the cylinder temperature is high. If the cylinder's temperature comes close to the temperature of the surrounding material, the temperature dependence of the viscosity is less helpful. Transferred to the diapir model it means that a colder diapir is of course slower than a hot one. Or extrapolated to a nonstationary model: A cooling diapir might become slower since it becomes progressively less able to reduce the viscosity and shear forces at its surface.

6. Conclusion

[37] This work was meant to determine the effect of a temperature dependent viscosity on the sinking of iron drops with a radius of a few kilometers. We found the effect to be remarkable, but the model still suffers from simplifications. The constant temperature of the diapirs is probably the most crucial one. We think that the results are still reasonable, because the enormous amount of internal energy an iron drop of 5 km has. To find out how much energy the diapir is releasing to the surrounding medium we could use the temperature distribution around the diapir at its terminal velocity and integrate the energy content of the "channel" over all finite elements. In a channel of the volume 100 km $\times$ 250 km $\times$ 10 km the diapir of 5 km radius looses 2.23×10^{10} J. If the diapir looses that amount of energy for very radius it sinks down, the total energy loss due to advection would be around 3×10^{13} J. We see that this value is negligible to the energy the diapir has because of its temperature. Note that any temperature rise due to release of potential energy is not even included. However, the energy loss is most certainly underestimated and does not include any heat loss due to friction in the silicate material. However, it shows that the cooling of an iron body of 5 km radius is not very effective and, albeit relatively simple, the assumption of a constant diapir temperature not too unrealistic in a first approach.

[38] Henceforth, our model does not give any details on the dynamics of the complete core formation process. A model for the differentiation of a full planet is yet to be developed. We want to point out that the times given in Table 2 should be read carefully. Because of the stationary character of our model we cannot say anything about the evolution of sinking velocity due to the change of the diapirs temperature. It is part of future study to find out, under what circumstances the conversion of potential energy is balanced by the heat loss due to advection and conduction. A better model will then include an energy balance, which takes release of potential energy, the heat loss due to dissipation, heat loss due to advection, etc., into account.

[39] **Acknowledgments.** We would like to thank Stefan Turek and the FEAST group, especially Rainer Schmachtel, Christian Becker and Dominik Gödekke, for the software. We thank further the reviewers P. Tackley and U. Christensen for their constructive suggestions, which helped improving the manuscript. This work was funded by the Deutsche Forschungsgemeinschaft.

References

Balog, P. S., R. A. Secco, D. C. Rubie, and D. J. Frost (2003), Equation of state of liquid Fe-10 wt % S: Implications for the metallic cores of planetary bodies, *J. Geophys. Res.*, *108*(B2), 2124, doi:10.1029/2001JB001646.

Batchelor, G. (1981), *An Introduction to Fluid Dynamics*, Cambridge Univ. Press, Cambridge, U. K.

Breuer, D. (2003), Thermal evolution, crustal growth and magnetic field history of Mars, habilitationschrift, Univ. Münster, Münster, Germany.

Bruhn, D., N. Groebner, and D. L. Kohlstedt (2000), An interconnected network of core-forming melts produced by shear deformation, *Nature*, *403*, 883–886.

Cathles, L. M. (1975), *The Viscosity of the Earth's Mantle*, Princeton Univ. Press, Princeton, N. J.

Folkner, W. M., C. F. Yoder, D. Yuan, E. M. Standish, and R. A. Preston (1997), Interior structure and seasonal Mass redistribution of Mars from radio tracking of Mars Pathfinder, *Science*, *278*, 1749–1752.

Holleman, A. F., and E. Wilberg (1985), *Lehrbuch der Anorganischen Chemie*, Walter de Gryter, New York.

Kahn, A., K. Mosegaard, and K. L. Rasmussen (2000), Lunar models obtained from a Monte Carlo inversion of the Apollo seismic P and S waves, *Lunar Planet. Sci. Conf.*, *XXXI*, Abstract 1341.

Kull, H. J. (1991), Theory of the Rayleigh-Taylor instability, *Phys. Rep.*, *206*, 197–325.

Larimer, J. W., and M. A. Herpfer (1994), An experimental study of core formation: metallic melt-silicate segregation, paper presented at Workshop on the formation of the Earth's core, Max-Planck-Inst. fr Chemie, Mainz, Germany.

Lodders, K., and B. Fegley (1998), *The Planetary Scientists Companion*, Oxford Univ. Press, New York.

Münker, C., J. A. Pfänder, S. Weyer, A. Büchl, T. Kleine, and K. Mezger (2003), Evolution of planetary cores and the Earth-Moon system from Nb/Ta systematics, *Science*, *301*, 84–87.

Palme, H., B. Spetteland, H. Wänke, A. Bischoff, and D. Stöffler (1984), Early differentiation of the Moon: Evidence from trace elements in plagioclase, *Lunar Planet. Sci. Lett., 15th, J. Geophys. Res.*, *89*, C3–C15.

Righter, K., and M. J. Drake (1996), Core formation in Earth's Moon, Mars and Vesta, *Icarus*, *124*, 513–529.

Rubie, D. C., H. Melosh, J. Reid, C. Liebske, and K. Righter (2003), Mechanisms of metal-silicate equilibration in the terrestrial magma ocean, *Earth Planet. Sci. Lett.*, *205*, 239–255.

Safronov, V. S. (1978), The heating of the Earth during its formation, *Icarus*, *33*, 3–12.

Schlichting, H. (1982), *Grenzschicht Theorie*, 8th ed., G. Braun, Karlsruhe, Germany.

Schmachtel, R. (2003), Robuste lineare und nichtlineare Lösungsverfahren für die inkompressiblen Navier-Stokes-Gleichungen, Ph.D. thesis, Fachber. Math., Univ. Dortmund, Dortmund, Germany.

Schubert, G., J. Anderson, T. Spohn, and W. McKinnon (2004), Interior composition, structure and dynamics of the Galilean satellites, in *Jupiter: The Planet, Satellites and Magnetosphere*, edited by F. Bagenal, T. E. Dowling, and W. B. McKinnon, pp. 281–307, Cambridge Univ. Press, Cambridge, U. K.

Sohl, F., and T. Spohn (1997), The interior structure of Mars: Implications from SNC meteorites, *J. Geophys. Res.*, *102*, 1613–1635.

Sohl, F., T. Spohn, D. Breuer, and K. Nagel (2002), Implications from galileo observations on the interior structure and chemistry of the galilean satellite, *Icarus*, *157*, 104–119.

Sommerfeld, A. (1992), *Mechanik der deformierbaren Materie*, 6th ed., Harry Deutsch, Frankfurt am Main, Germany.
Spohn, T., F. Sohl, K. Wieczerkowski, and V. Conzelmann (2001), The interior structure of mercury: What we know, what we expect from bepicolombo, *Planet. Space Sci.*, *49*, 1561–1570.
Stephenson, A., S. Runcorn, and D. Collinson (1975), On changes in the intensity of the ancient lunar magnetic field, *Lunar Planet. Sci. Conf.*, *6*, 3049–3062.
Stevenson, D. J. (1989), Formation and early evolution of the Earth, in *Mantle Convection*, edited by W. Peltier, pp. 817–873, Gordon and Breach, New York.
Stevenson, D. J. (1990), Fluid dynamics of core formation, in *Origin of the Earth*, edited by H. Newsom and J. Jones, pp. 231–249, Oxford Univ. Press, New York.
Stevenson, D. J., T. Spohn, and G. Schubert (1983), Magnetism and Thermal Evolution of the Terrestrial Planets, *Icarus*, *54*, 466–489.
Stöcker, H. (1994), *Taschenbuch der Physik*, Harry Deutsch, Frankfurt am Main, Germany.
Trottenberg, U., C. Oosterlee, and A. Schüller (2001), *Multigrid*, Academic, London.
Turcotte, D., and G. Schubert (2002), *Geodynamics*, 2nd ed., John Wiley, London.
Turek, S. (1998), *Efficient solvers for inkompressible flow problems: An algorithmic approach in view of computational aspects*, Springer, Heidelberg, Germany.
van Bargen, N., and H. S. Waff (1986), Permeabilities, interfacial areas and curvatures of partially molten systems: Results of numerical computations of equilibrium microstructures, *J. Geophys. Res.*, *91*, 9261–9276.
van den Berg, A. P., and D. A. Yuen (2002), Delayed cooling of the Earth's mantle due to variable thermal conductivity and the formation of a low conductivity zone, *Earth Planet. Sci. Lett.*, *199*, 403–413.
van den Berg, A. P., D. A. Yuen, and V. Steinbach (2001), The Effects of variable themal conductivity on mantle heat-transfer, *Geophys. Res. Lett.*, *28*, 875–878.
Wänke, H., et al. (1977), On the chemistry of lunar samples and chondrites. Primary matter in the lunar highlands: A re-evaluation, *Lunar Planet. Sci. Conf.*, *8*, 2191–2213.
Wesseling, P. (1992), *An Introduction to Multigrid Methods*, John Wiley, London.
Whitehead, J. A., and D. S. Luther (1975), Dynamics of laboratory diapir and plume models, *J. Geophys. Res.*, *80*, 705–717.
Woidt, W. D. (1978), Finite element calculations applied to salt dome analysis, *Tectonophysics*, *50*, 369–386.
Yoder, C. F., A. S. Konopliv, D. N. Yuan, E. M. Standish, and W. M. Folkner (2003), Fluid core size of Mars from detection of the solar tide, *Science*, *300*, 299–303.
Yoshino, T., M. Walter, and T. Katsura (2003), Core formation in planetesimals triggered by permeable flow, *Nature*, *422*.
Zahnle, K. J., J. G. Kasting, and J. B. Pollack (2003), Evolution of a steam atmosphere during Earth's accretion, *Icarus*, *74*, 62–97.

T. Spohn, Deutsches Zentrum für Luft- und Raumfahrt in der Helmholtz Gemeinschaft, Institut für Planetenforschung, Rutherfordstrasse 2, D-12489 Berlin, Germany.

R. Ziethe, Institute of Physics, University of Berne, Sidlerstr. 5, CH-3012 Bern, Switzerland. (ziethe@space.unibe.ch)